Nanoscale

PAPER

View Article Online
View Journal

Check for updates

Cite this: DOI: 10.1039/d6nr00517a

Conduction mode transition in Ag nanowire–mesh hybrid electrodes by junction welding for high-performance transparent conductive electrodes

Seung Taek Jo,[a] Chan Woong Kim,[a] Jin Wook Shin,[a] Gyeongtae Kim,[a] Dongrim Lee,[b] Dae-Hwang Yoo,[c] Hyesun Yoo *[c] and Jong Wook Roh *[a,c,d]

Received 6th February 2026,
Accepted 12th May 2026

DOI: 10.1039/d6nr00517a

rsc.li/nanoscale

While hybrid transparent conductive electrodes (TCEs) that combine silver nanowires (Ag NWs) with metal mesh frameworks have emerged as promising alternatives to other transparent electrode materials such as carbon-based materials, conductive polymers, and indium tin oxide (ITO), their performance remains constrained by high contact resistance at junctions between NWs and metal mesh interfaces. This study demonstrates that thermal welding at 200 °C for 10 min both reduces the contact resistance and fundamentally alters the conduction behavior of Ag mesh/Ag NW hybrid electrodes from a percolative regime to a bulk-like regime. This transition shifts the dominant factor governing the figure of merit (FoM) from sheet resistance to optical transmittance. As a result, even with a minimal Ag NW concentration, the welded hybrid electrodes achieve a sheet resistance of 7 Ω sq^{-1}, a transmittance of 86.1% at 550 nm, and an FoM of 373, thereby rivaling commercial ITO. Furthermore, a systematic analysis of the mesh density and Ag NW coverage reveals distinct conduction sensitivities depending on pitch. These findings highlight the potential of contact-engineered conduction mode switching as a design principle for high-efficiency, low-cost TCEs, offering a scalable pathway toward next-generation optoelectronic and flexible devices.

Open Access Article. Published on 13 May 2026. Downloaded on 6/28/2026 9:54:55 AM.
This article is licensed under a Creative Commons Attribution-NonCommercial 3.0 Unported Licence.

Introduction

Transparent conductive electrodes (TCEs) are essential components in next-generation optoelectronic devices such as touch panels,[1,2] solar cells,[3,4] and transparent heaters.[5,6] For commercialization, TCEs must simultaneously exhibit high optical transmittance (>85%) and low sheet resistance (<10 Ω sq^{-1}). Indium tin oxide (ITO) remains the dominant material due to its excellent optoelectronic properties; however, its cost-effective deployment over large-area applications and its use in flexible devices are limited by its reliance on the scarce and costly element indium, along with its intrinsic brittleness. To overcome these limitations, alternative electrodes such as silver nanowires (Ag NWs),[7,8] metal meshes,[9,10] and carbon nanotubes (CNTs)[11,12] have been investigated. Among these, CNT electrodes offer flexibility and chemical stability, but their high junction resistance and limited conductivity result in poor sheet resistance and high fabrication costs.[13] Meanwhile, metal meshes provide low resistance and scalable fabrication, but their transparency–resistance performance is constrained by the intrinsic trade-off between pitch and line width.[14] Conversely, Ag NWs deliver superior optical and electrical performances due to their low percolation threshold and high aspect ratio, but their standalone performance is restricted by the junction resistance between individual NWs.[15] Hence, hybrid electrodes that combine metal meshes and Ag NWs have been proposed in order to take advantage of the long-range conduction pathways provided by the mesh, while reducing the overall resistance by using NWs to bridge the gaps between mesh lines.[16–18]

Various hybrid electrode fabrication methods have been reported, including inkjet printing,[19] nanoimprint lithography,[20] and screen printing.[21] However, the majority of studies have emphasized processing and mechanical stability rather than systematically addressing conduction regimes. In particular, the relationship between mesh pitch and NW length, and how this governs the transition between percolation-dominated and bulk-like conduction regimes, remains poorly understood. Meanwhile, the limitations of NWs can be addressed by welding, which reduces the junction resistance by forming conductive bridges between individual NWs.[22–24]

[a]Department of Hydrogen and Renewable Energy, Kyungpook National University, Daegu 41556, Republic of Korea. E-mail: jw.roh@knu.ac.kr
[b]Department of Energy Convergence and Climate Change, Kyungpook National University, Daegu 41556, Republic of Korea
[c]Regional Leading Research Center (RLRC) of Smart Energy System, Kyungpook National University, Gyeongsangbuk-do 37224, Republic of Korea. E-mail: vorahsun@gmail.com
[d]School of Nano and Materials Science and Engineering, Kyungpook National University, Gyeongsangbuk-do 37224, Republic of Korea

Open Access Article. Published on 13 May 2026. Downloaded on 6/28/2026 9:54:55 AM.
This article is licensed under a Creative Commons Attribution-NonCommercial 3.0 Unported Licence.

Thermal annealing,[25] cold welding,[26] and hot pressing[27] have been widely studied and shown to improve the figure of merit (FoM) of percolative electrodes. For instance, Xu *et al.* reported that cold welding enhances the FoM of percolative electrodes more effectively than bulk-like electrodes, underscoring the critical role of junction resistance close to the percolation threshold.[28] Similarly, Langley *et al.* showed that thermal annealing promotes the formation of additional conduction pathways at NW junctions.[29] Nevertheless, despite these advances, little is known about the effect of welding on the conduction modes of hybrid electrodes, where both percolation and mesh-assisted transport coexist.

In this study, Ag micro-meshes with systematically varied pitches (low, medium, and high density) are fabricated *via* a cracked-template process, then coated with Ag NWs and subjected to thermal welding at 200 °C for 10 min. By tuning the ratio between mesh pitch and average NW length, the conditions under which the sheet resistance can be minimized with minimal NW usage are identified. Notably, when the mesh pitch closely matches the NW length, the hybrid electrode achieves an FoM of 373, along with a sheet resistance as low as 7.0 Ω sq^{-1} at 86.1% transmittance, thereby outperforming commercial ITO. These results demonstrate that pitch–length matching, combined with junction welding, modulates the dominant conduction pathways in hybrid electrodes, providing a mechanistic framework for the rational design of high-performance TCEs. This work establishes practical design rules and processing strategies for flexible, low-cost transparent conductors suitable for emerging optoelectronic applications.

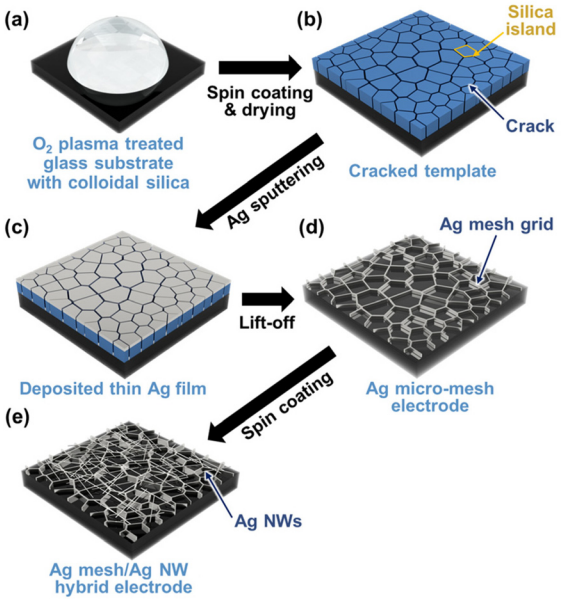

Fig. 1 A schematic illustration of the fabrication processes for the Ag micro-mesh and Ag micro-mesh/Ag NW hybrid electrodes. Here, colloidal silica is spin-coated onto a glass substrate (a) at various speeds to produce cracked templates (b) with controlled mesh thickness and pitch. This is followed by Ag sputtering (c) and lift-off to obtain an Ag micro-mesh grid (d). After that, Ag NWs are spin-coated onto the micro-mesh surface (e), and the sample is subjected to heat treatment at 200 °C for 10 min to induce welding between the Ag NWs and mesh lines.

Experimental

The fabrication of the Ag micro-mesh and hybrid Ag micro-mesh/Ag NW electrode is shown schematically in Fig. 1 First, a soda-lime glass substrate (25 × 25 × 0.7 mm^3) was sequentially cleaned in acetone, ethanol, and deionized (DI) water *via* ultrasonication for 30 min each, and then dried in an oven at 80 °C for 10 min to remove any residual moisture (Fig. 1a). After that, the cleaned glass substrate was treated with O_2 plasma at 100 W power for 30 s to increase hydrophilicity, followed by the application of a colloidal silica solution (Ludox HS-30, Sigma-Aldrich) *via* spin coating (SE-100LED, RHABDOS SPINCOATER) for 30 s and subsequent drying for 10 min at room temperature with a relative humidity of 20–30% to obtain a cracked template (Fig. 1b). The structure of the resulting spin-coated sample is shown in the surface and cross-sectional SEM images in Fig. S1a and b, respectively. The structure of this cracked template, which determines the density of the Ag micro-mesh pattern, was controlled by using spin-coating speeds of 2000, 4000, and 6000 rpm to vary the sizes of the silica islands. The resulting low-, medium-, and high-density meshes are referred to hereafter as the LD-mesh, MD-mesh, and HD-mesh, respectively. An ~120 nm-thick Ag thin film was then deposited onto the cracked template by using radio frequency (RF) magnetron sputtering (Fig. 1c). After that, the sample was immersed in DI water and ultrasonically cleaned for 10 min to remove ("lift off") the silica islands from the glass substrate, leaving only the Ag thin film tracing out the pattern of cracks on the glass substrate (Fig. 1d). This completed the fabrication process of the basic Ag micro-mesh electrode (Fig. S1c). To obtain the hybrid electrodes, Ag NWs with an average length of 25 μm and diameter of 25 nm (Flexiowire2020a, 0.5 wt% in DI water, SGFLEXIO) were subsequently deposited onto the surfaces of the LD-, MD-, and HD-mesh samples by the same spin coating process at various speeds (Fig. 1e). Specifically, Ag NW spin-coating speeds of 1000, 2000, 3000, 4000, 5000 and 6000 rpm were applied to the LD-, MD-, and HD-meshes to obtain the hybrid samples designated as LD-mesh_Ag1000, *etc*. As shown in Fig. S1d, the Ag NWs were well deposited in the empty spaces between the Ag micro-mesh network. Finally, to improve the Ag NW/Ag NW and Ag micro-mesh/Ag NW contact resistance, a welding process was performed by heat treating the samples on a hotplate at 200 °C for 10 min. In addition, Ag NW-only electrodes were prepared by spin coating the Ag NWs directly onto soda-lime glass substrates at speeds of 1000, 2000, 3000, 4000, 5000, and 6000 rpm; the resulting samples are designated hereafter as Ag1000, Ag2000, Ag3000, Ag4000, Ag5000, and Ag6000, respectively.

The pitch and width of the Ag micro-mesh and the distributions of Ag NWs in the hybrid samples were examined *via*

This journal is © The Royal Society of Chemistry 2026

Open Access Article. Published on 13 May 2026. Downloaded on 6/28/2026 9:54:55 AM.
This article is licensed under a Creative Commons Attribution-NonCommercial 3.0 Unported Licence.

field-emission scanning electron microscopy (FE-SEM, Regulus 8220, HITACHI). In addition, the surface resistivity was measured at three different locations by using a four-point probe surface resistivity meter (RC2175, RDTM), and the average value was calculated. The transmittance at a wavelength of 550 nm was also measured at three points by using a spectrophotometer (Spectro 22RS, Labomed), and the average was recorded. In addition, the full UV-visible (UV-vis.) transmittance spectra (380–800 nm) were measured using a UV-VIS-NIR spectrophotometer (UV-3600i Plus, Shimadzu) to evaluate the wavelength-dependent optical properties of the hybrid electrodes. The measured average sheet resistance (R_s) and transmittance (T) were then used to calculate the figure of merit (FoM) of each TCE by using the formula given in eqn (1):[30]

$$\mathrm{FoM} = \frac{\sigma_{DC}}{\sigma_{op}} = \frac{188.5}{R_s\left(\frac{1}{\sqrt{T}} - 1\right)} \quad (1)$$

where σ_{DC} is the DC conductivity and σ_{op} is the optical conductivity of the electrodes. The measured sheet resistance and transmittance values were used to plot a graph of $(1/\sqrt{T} - 1)$ *versus* R_s on a log–log scale, and the slope was calculated in order to evaluate the conductive properties of the hybrid electrodes. The percolation exponent n was then determined using the slope and the relevant formula, as given in eqn (2):

$$T = \left[1 + \frac{1}{\Pi}\left(\frac{Z_0}{R_s}\right)^{\frac{1}{n+1}}\right]^{-2} \quad (2)$$

where Z_0 is the free-space impedance (188.5), Π is the percolative figure of merit (FoM), and n is the percolation exponent. The calculation results are summarized in Table S1. Additionally, to confirm the formation of junctions between the Ag NWs during welding, the thickness of Ag NWs before and after welding was measured by using atomic force microscopy (AFM; Park Systems, XE-70).

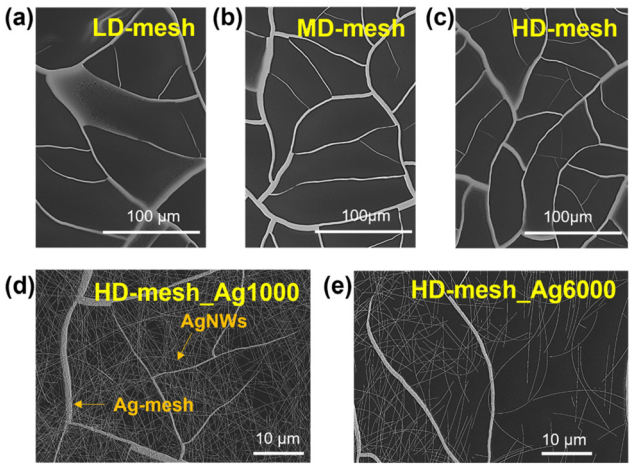

Fig. 2 (a–c) SEM surface images of Ag micro-mesh electrodes with different pitches depending on the spin-coating speed used to form a cracked template: (a) the LD-mesh, (b) the MD-mesh, and (c) the HD-mesh. (d and e) SEM images of the hybrid electrodes after coating with Ag NWs at (d) 1000 rpm and (e) 6000 rpm on the HD-mesh, illustrating the changes in NW density on the mesh surface.

Results and discussion

The surface structures of the pristine LD-, MD-, and HD-mesh electrodes are revealed by the SEM images in Fig. 2a–c. Here, the LD-mesh exhibits a sparsely distributed network with relatively broad lines, whereas the HD-mesh exhibits a denser network with narrower lines. Thus, as summarized in Table 1, the average width and pitch of the Ag micro-mesh decrease from 4.75 to 2.62 μm and 50.9 to 27.2 μm, respectively, as the spin-coating speed increases from 2000 rpm (LD) to 6000 rpm (HD). To understand how these structural differences affect the electrical and optical properties, the sheet resistance and transmittance at a wavelength of 550 nm were measured for each sample. The results in Table 1 show that the sheet resistance increases from 7.0 to 25.0 Ω sq^{-1}, while the transmittance increases from 79.1% to 90.1%, as the mesh density increases on going from the LD-mesh to the HD-mesh samples. This indicates that while the cross-sectional area available for current flow decreases as the area coverage of the metal electrode within the mesh structure decreases, the optical transmission pathway increases. Furthermore, when comparing the average width and pitch values of the network, it can be seen that changes in width have a more direct impact on the electrode's coverage and sheet resistance characteristics.

Meanwhile, the electrical and optical properties of the various Ag NW-only samples (Ag1000–6000) are summarized in Fig. S3, while the surface distributions of Ag NWs in each sample are shown by the SEM images in Fig. S2. Thus, with an increase in spin-coating speed, the density of NWs is seen to decrease gradually, while the sheet resistance increases from 58.8 to 84.5 Ω sq^{-1}, and the transmittance increases from 91.1% to 98.4%. Notably, when comparing the six samples,

Table 1 The width, pitch, sheet resistance, and transmittance values of the pristine LD-, MD-, and HD-meshes

Mesh density	Spin-coating speed (rpm)	Width (μm)	Pitch (μm)	Sheet resistance (R_s; Ω sq^{-1})	Transmittance (T; %)
Low (LD)	2000	4.75	50.9	7.0	79.1
Medium (MD)	4000	3.22	34.6	17.3	88.7
High (HD)	6000	2.62	27.2	25.0	90.1

Open Access Article. Published on 13 May 2026. Downloaded on 6/28/2026 9:54:55 AM.
This article is licensed under a Creative Commons Attribution-NonCommercial 3.0 Unported Licence.

the difference in transmittance is relatively gradual, whereas the sheet resistance shows a more pronounced variation. In particular, the largest increase in sheet resistance occurs between Ag3000 (at 66.8 Ω sq^{-1}) and Ag4000 (76.3 Ω sq^{-1}), thereby suggesting that this range plays a critical role in the formation of the conductive pathway.

Based on the confirmed electrical and optical properties of the Ag NW-only electrodes, the same procedure was used to deposit Ag NWs onto the LD-, MD-, and HD-mesh electrodes to obtain the hybrid electrode structures shown in Fig. 2d and e, and Fig. S2. The corresponding sheet resistance and transmittance measurements are shown in Fig. 3a and b, respectively. Here, the introduction of Ag NWs into each mesh type leads to a decrease in sheet resistance compared to that of the corresponding mesh-only sample (Table 1). This is interpreted as the Ag NWs effectively bridging the open areas between the mesh lines to create additional electron transport pathways, thereby enhancing the overall conductivity. For example, in the case of the MD-mesh, the sheet resistance decreases from 17.3 Ω sq^{-1} for the mesh-only electrode to 7.8 Ω sq^{-1} for the MD-mesh_Ag1000 electrode. Similarly, the sheet resistance of the LD-mesh and HD-mesh samples decreases from 7.0 to 4.3 Ω sq^{-1} and from 25.0 to 10.4 Ω sq^{-1}, respectively, upon the addition of Ag NWs at a spin-coating speed of 1000 rpm. Moreover, the sheet resistance values of the hybrid electrodes are even lower than those of the Ag NW-only electrodes (Fig. S3a), which clearly demonstrates the electrical synergy between the mesh and NW structures.

The results in Fig. 3a also indicate that the sheet resistance of the hybrid electrode tends to increase as the spin-coating speed of the Ag NWs increases (*i.e.*, as the density of Ag NWs decreases). This phenomenon is similar to that observed in the NW-only electrodes (Fig. S3a) and is interpreted as a weakening of the bridging pathways due to the reduced density of Ag NWs. Specifically, the sheet resistance of the LD-mesh_hybrid electrode (black profile, Fig. 3a) increases by about 47%, from 4.3 Ω sq^{-1} at an Ag NW spin-coating speed of 1000 rpm (LD-mesh_Ag1000) to 6.3 Ω sq^{-1} at an Ag NW spin-coating speed of 6000 rpm (LD-mesh_Ag6000). In the case of the HD-mesh_hybrid electrode (blue profile), however, a relatively moderate increase of around 15% is observed, from 10.4 Ω sq^{-1} (HD-mesh_Ag1000) to 12.0 Ω sq^{-1} (HD-mesh_Ag6000), under the same conditions. Similarly, an increase of around 21% is observed for the MD-mesh_hybrid electrode (red profile). In other words, the LD-mesh-based hybrid electrode is more sensitive to changes in the density of Ag NWs compared

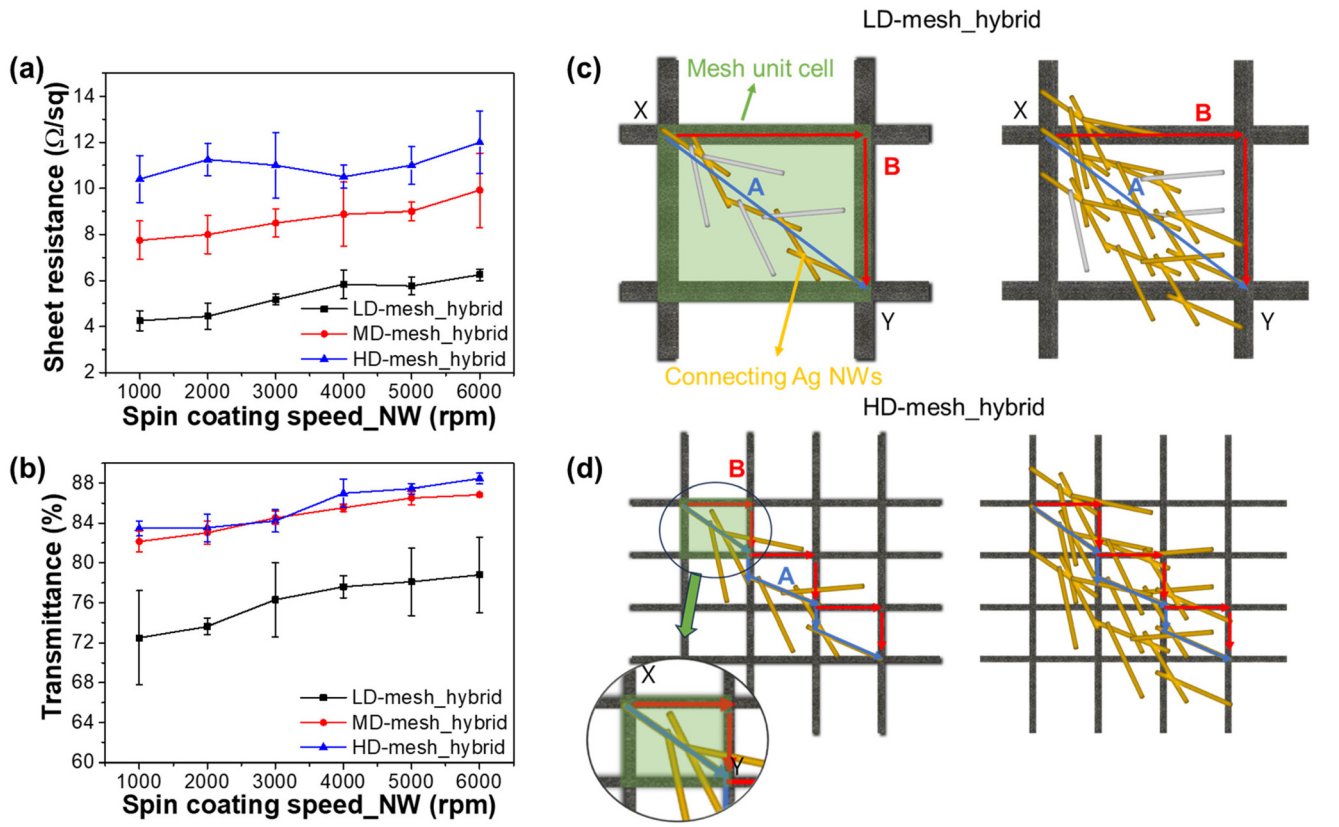

Fig. 3 (a and b) The sheet resistance (a) and transmittance (b) of the LD-, MD-, and HD-mesh hybrid electrodes as a function of Ag NW coating speed. (c and d) Schematic diagrams showing current pathways in the hybrid LD-mesh (c) and HD-mesh (d) samples. Here, electrons are transported either *via* the Ag NWs that connect neighboring mesh lines (path A) or through the mesh lines themselves (path B). When the mesh pitch closely matches the Ag NW length, effective conduction through path A is enabled even at relatively low NW densities.

Open Access Article. Published on 13 May 2026. Downloaded on 6/28/2026 9:54:55 AM.
This article is licensed under a Creative Commons Attribution-NonCommercial 3.0 Unported Licence.

to the other hybrid electrodes. This difference is attributed to the varying relative influence of the auxiliary conductive pathways contributed by the Ag NWs depending on the density (pitch) of the mesh network. Thus, the wider pitch of the LD-mesh structure allows the Ag NWs to play a crucial role in the formation of conductive pathways, whereas the narrower pitch of the dense HD-mesh structure allows the Ag NWs to make only a smaller contribution.

The above differences in conduction mechanisms are visualized by the schematic current flow pathways within the LD-mesh_hybrid in Fig. 3c. Here, the pathway is shown based on the current flow from point X, where two mesh lines intersect, to point Y. The rectangular area enclosed by the mesh lines is defined as a single mesh unit cell, which is highlighted by the green square (left panel of Fig. 3c). Within this unit cell, Ag NWs that directly connect opposing mesh lines and contribute to current flow are classified as connecting NWs and emphasized in yellow. In contrast, dangling or isolated NWs that are distributed around but do not participate in forming the main current pathway are classified as non-connecting Ag NWs and are shown in white. Current can flow through this unit cell *via* two primary paths. One follows the connections formed by the Ag NWs (path A, blue line), while the other follows the existing Ag mesh lines (path B, red line). Based on the schematic shown in the left panel of Fig. 3c, the resistance associated with a single Ag NW-mediated connecting path, formed by the connecting NWs bridging points X and Y, is defined as R_A. This resistance can be expressed by eqn (3), which accounts for the contributions from individual NW segments and their contact resistances. Similarly, the resistance of the mesh-line pathway is defined as R_B and can be described by eqn (4):

$$R_A = nR_{NW} + (n-1)R_{C\cdot NWs} + kR_{C\cdot hybrid} \quad (3)$$

$$R_B = R_{mesh} \quad (4)$$

where R_{mesh} and R_{NW} are the resistance values of the mesh and a single NW, respectively, $R_{C\cdot NWs}$ is the contact resistance between individual NWs, and $R_{C\cdot hybrid}$ is the contact resistance between the NWs and the mesh. The parameter n represents the estimated number of connecting NWs in a single Ag NW-mediated connecting path, which can be roughly approximated as the mesh pitch divided by the NW length (assuming random orientation). The parameter k represents the number of contact points between the nanowires and the mesh lines within a single path. Thus, eqn (3) describes the cumulative resistance of a single Ag NW-mediated connecting path, which includes the resistance of each individual NW, the contact resistance between neighboring NWs, and the contact resistance between NWs and the mesh, whereas the simpler eqn (4) represents the resistance of a single pathway through the mesh line only.

As the number of Ag NW-mediated connecting paths between mesh lines increases (right panel of Fig. 3c), the total connecting paths from X to Y through the Ag NWs (path A) can be assumed to operate like parallel circuits. For simplification, assuming that each connecting path has the same resistance (R_A), the equivalent resistance of m parallel connecting paths ($R_{A,eq}$) can be expressed by eqn (5):

$$\frac{1}{R_{A,eq}} = \frac{1}{R_A} + \frac{1}{R_A} + \frac{1}{R_A} \cdots = \frac{m}{R_A} \quad (5)$$

where m is the number of Ag NW-mediated connecting paths that directly link the mesh lines within a mesh unit cell, which is closely related to the distribution density of the Ag NWs. By substituting the expression for R_A from eqn (3) into eqn (5), the $R_{A,eq}$ can be rewritten as eqn (6):

$$R_{A,eq} = \frac{R_A}{m} = \frac{nR_{NW} + (n-1)R_{C\cdot NWs} + kR_{C\cdot hybrid}}{m} \quad (6)$$

Because R_{NW} corresponds to the resistance of an individual NW, it generally has a relatively small value compared with each type of contact resistance. Therefore, the equivalent resistance in eqn (6) is mainly dominated by the contact resistance values ($R_{C\cdot NWs}$ and $R_{C\cdot hybrid}$). Furthermore, when the value of m is small, the number of parallel paths is limited, so $R_{A,eq}$ is greatly affected by the contact resistance. As a result, the relative contribution of path B becomes dominant. Conversely, as the density of Ag NWs increases and m becomes sufficiently large, the number of parallel paths increases, which leads to a sharp decrease in the effective resistance of path A. As a result, especially in structures such as the LD-mesh, with its wide pitch, the contribution of path A gradually increases, and the current flows more efficiently both through the mesh lines and along the auxiliary paths formed by the Ag NWs. In the case of the HD-mesh (Fig. 3d), however, the pitch (27.2 μm) is similar to the length of the individual Ag NWs (~25 μm). This implies that n approaches 1, effectively minimizing the contribution of $R_{C\cdot NWs}$ even at low NW densities. This means that the HD-mesh hybrid electrode can effectively reduce the sheet resistance with only a small quantity of Ag NWs because the conduction pathway does not change significantly with variations in NW density. Consequently, more effective parallel paths are established early on, leading to a lower and more stable sheet resistance compared with the LD-mesh, regardless of variations in NW density.

While the sheet resistance values of the hybrid electrodes in Fig. 3a show a clear change depending on the mesh pitch and density of Ag NWs, the corresponding transmittance values (Fig. 3b) are relatively unaffected. For example, the LD-mesh_Ag1000, MD-mesh_Ag1000, and HD-mesh_Ag1000 samples exhibit transmittance values of 72.5%, 82.2%, and 83.5%, respectively, compared to 79.1%, 88.7%, and 90.1% for the corresponding mesh-only samples (Table 1 and Fig. S3b). This represents reductions of only 5–6% with the introduction of the Ag NWs at 1000 rpm, compared to the abovementioned 15–47% variations in sheet resistance. Additionally, increasing the Ag NW spin-coating speed from 1000 to 6000 rpm leads to only slight increases in transmittance (around 6–9%). For example, in the case of the LD-mesh hybrid, the transmittance increases by about 8.7%, from 72.5% (LD-mesh_Ag1000) to 78.8% (LD-mesh_Ag6000), while that of the HD-mesh_hybrid

Open Access Article. Published on 13 May 2026. Downloaded on 6/28/2026 9:54:55 AM.
This article is licensed under a Creative Commons Attribution-NonCommercial 3.0 Unported Licence.

increases by about 6%, from 83.5% to 88.5%. Considering that the transmittance of the standalone Ag NW electrode ranges from 91.1% for Ag1000 to 98.4% for Ag6000 (Fig. S3b), the differences in transmittance observed in the hybrid electrodes can be attributed to the surface coverage area of the Ag NWs. This behavior indicates that the optical loss induced by the Ag NWs, arising from light absorption and scattering, contributes in a consistent manner regardless of the mesh structure. To further assess the optical characteristics beyond a single wavelength, the full UV-visible transmittance spectra (380–800 nm) of representative hybrid electrodes after welding were measured and are shown in Fig. S4. The spectra exhibit broad and relatively moderate visible range variation without a pronounced sharp wavelength-selective dip. Compared with many reported Ag NW-containing transparent electrodes,[23–26] the present Ag mesh/Ag NW hybrid electrodes show less pronounced spectral variation, which is likely attributable to the lower effective Ag NW density and the broadband optical contribution of the Ag mesh, whose transmittance is governed mainly by geometric open-area effects rather than strongly wavelength-dependent absorption.

As described by eqn (6), the lower Ag NW density in the hybrid electrode corresponds to a reduced value of m, thereby enhancing the relative influence of contact resistance on the overall sheet resistance. This implies that the contact resistance increasingly constrains the available current pathways and, consequently, contributes to an increase in sheet resistance. Conversely, if the contact resistance can be effectively reduced, then even hybrid electrodes with low densities of Ag NWs can be expected to achieve a sufficiently low sheet resistance. To verify this, the various hybrid electrode samples were heat-treated at 200 °C for 10 min to induce thermal welding between the Ag NWs, and the effect is clearly revealed by the SEM images in Fig. 4a and b. Thus, compared to the image obtained before welding (Fig. 4a), the areas indicated by the yellow circles in the heat-treated sample (Fig. 4b) distinctly exhibit multiple Ag NWs welded together to form a continuous, integrated structure. Furthermore, this phenomenon is quantitatively verified at the nanoscale by the AFM images in Fig. S5. Thus, before welding (Fig. S5a–c), the thickness of area A, where two NWs overlap, is 43.7 nm, which is approximately twice that of area B (21.7 nm), which contains a single NW. After welding (Fig. S5d–f), however, the thickness of area A in Fig. S5e and f (with overlapping NWs) decreases to 34.5 nm, which is not significantly different from the thicknesses of areas B and C with single NWs (23.7–30.0 nm). These results indicate that the overlapping NWs become fused together during the welding process to form a single layer, thereby creating an electrically continuous network. This welding effect is directly linked to the reduction of $R_{A,eq}$ in eqn (6). Before heat treatment, the contact resistance significantly contributes to $R_{A,eq}$, thereby limiting the current pathways. After welding, however, the contact resistance is markedly reduced, thus leading to a decrease in $R_{A,eq}$ and allowing current to flow

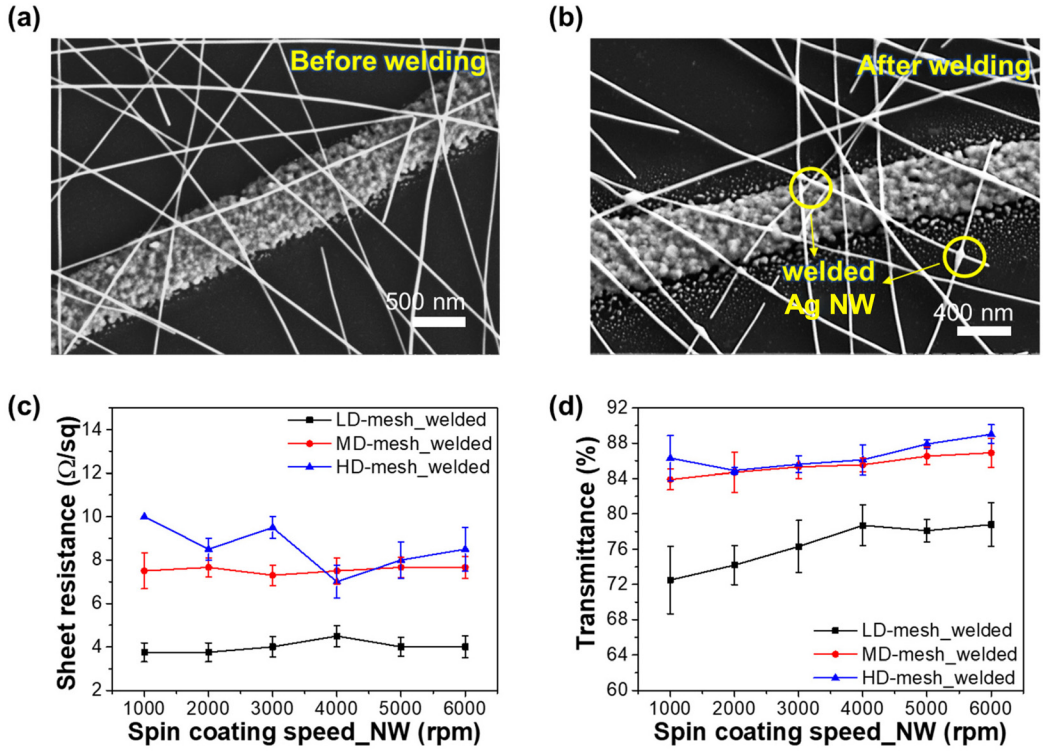

Fig. 4 (a and b) SEM images of an Ag mesh–Ag NW hybrid electrode (a) before and (b) after heat treatment (welding) at 200 °C for 10 min. The yellow circles in part (b) indicate welded junctions where the Ag NWs are integrated with the mesh lines or with other Ag NWs. (c and d) The sheet resistance (c) and transmittance at 550 nm (d) of the welded LD-, MD-, and HD-mesh hybrid electrodes as a function of Ag NW coating speed.

This journal is © The Royal Society of Chemistry 2026

Open Access Article. Published on 13 May 2026. Downloaded on 6/28/2026 9:54:55 AM.
This article is licensed under a Creative Commons Attribution-NonCommercial 3.0 Unported Licence.

through various pathways. As a result, the number of effective conductive pathways within the hybrid electrode increases, and the overall sheet resistance is significantly lowered. This is consistent with previous reports on Ag NW networks, where localized welding induced by heat treatment has been shown to cause a sharp decrease in the junction contact resistance.[29,31] For instance, Langley *et al.* reported that sintering at the NW junctions progresses during heat treatment at 200–300 °C, thereby increasing the number of effective conductive pathways within the network and reducing the overall sheet resistance by more than an order of magnitude.[29]

In fact, by comparing the results in Fig. 4c with those in Fig. 3a, it can be seen that the sheet resistance of the LD-mesh_Ag6000 sample decreases from 6.3 Ω sq^{-1} before welding (Fig. 3a) to 4.0 Ω sq^{-1} after welding (Fig. 4c). Similarly, the sheet resistance of the MD-mesh_Ag6000 decreases from 9.9 Ω sq^{-1} before welding to 7.7 Ω sq^{-1} afterwards, while that of the HD-mesh_Ag6000 decreases from 12.0 to 8.5 Ω sq^{-1}. More notably, whereas the non-welded hybrid electrodes exhibit a clear dependence of sheet resistance on Ag NW density, this dependence almost completely disappeared after the heat treatment. For example, in the case of the welded LD-mesh (Fig. 4c), even as the Ag NW coating speed increases from 1000 to 6000 rpm, the sheet resistance remains within the range of 3.8 to 4.5 Ω sq^{-1}. Similarly, the welded MD- and HD-meshes show only limited changes within the ranges of 7.3–7.7 Ω sq^{-1} and 7.0–10.0 Ω sq^{-1}, respectively. This indicates that, because welding greatly reduces the contact resistance between NW–NW and NW–mesh junctions, the changes in conductive pathways due to Ag NW density no longer play a major role. In other words, unlike the non-welded hybrid electrodes, where a lower Ag NW density accentuates the effect of contact resistance, the reduction in contact resistance in each welded electrode stabilizes the current pathways and effectively offsets the effects of density variation. The above results provide important implications for the design of hybrid electrodes. While simply increasing the density of Ag NWs may lead to a loss in transmittance, effective control of the contact resistance by welding can provide a sufficiently low sheet resistance even under low-density conditions. Therefore, this study clearly demonstrates that, along with the design of the mesh structure and control of the Ag NW distribution, post-treatment strategies for reducing the contact resistance play a crucial role in optimizing the performance of hybrid electrodes.

Fig. 5 shows the comparison of the figure of merit (FoM) of the hybrid electrodes before and after the welding process, thereby revealing how the dominant performance factors of the TCEs are shifted. Specifically, before welding (Fig. 5a), the various mesh_hybrid samples show relatively little variation in their FoM values depending on the density of Ag NWs. Quantitatively, the FoM values of the LD-mesh_hybrid and MD-mesh_hybrid samples remain within the narrow ranges of 238–257 and 235–279, respectively, while that of the HD-mesh_hybrid exhibits a relatively wider distribution of 178–249, remaining at around 180 at high NW densities (1000–3000 rpm) and approximately 250 at low NW densities (4000–6000 rpm). This tendency towards consistent FoM values couldcan be explained by the conduction behavior discussed earlier in Fig. 3a and b. There, while the transmittance is seen to increase as the Ag NW density decreases with increasing spin-coating speed (1000–6000 rpm), the sheet resistance is also increased. These two effects tend to offset each other, thereby causing the FoM to remain relatively unaffected by the NW density and to remain at similar levels. In other words, for the mesh_hybrid electrodes, the FoM is more strongly determined by the fundamental structural characteristics of the mesh (such as width and pitch) rather than the density of Ag NWs. After welding, however, a clear difference is observed (Fig. 5b). In this case, the FoM tends to increase gradually from 288 to 372 for the LD-mesh_welded samples, from 252 to 337 for the MD-mesh_welded samples, and from 199 to 373 for the HD-mesh_welded samples. Notably, the HD-mesh_welded electrode at Ag4000 achieves a low sheet resistance of 7 Ω sq^{-1} and a high transmittance of 86.1% with only

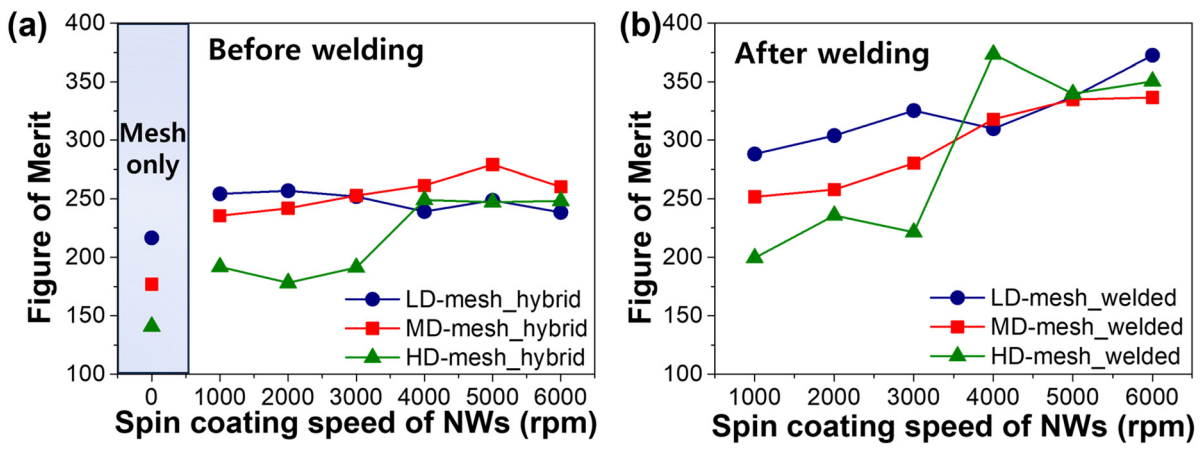

Fig. 5 Plots of the figure of merit (FoM) values of various hybrid electrodes as a function of Ag NW coating speed (a) before and (b) after welding, along with the FoM values of the corresponding mesh-only electrodes (*i.e.*, without Ag NWs).

Open Access Article. Published on 13 May 2026. Downloaded on 6/28/2026 9:54:55 AM.
This article is licensed under a Creative Commons Attribution-NonCommercial 3.0 Unported Licence.

a relatively small quantity of NWs, resulting in a maximum FoM of 373. This value is highly competitive even compared to commercial ITO-based electrodes, thereby indicating that the welding process is a critical step from a practical design perspective. The increase in FoM with decreasing Ag NW density can be further elucidated by examining the results in Fig. 4c and d. Since the NW–NW and NW–mesh contact resistances in the welded samples are reduced compared to those of the corresponding non-welded samples, the sheet resistance of the welded samples remains stable regardless of the Ag NW density. This signifies that the improved FoM of the welded samples is primarily driven by improvements in transmittance (Fig. 4d), which ultimately reflects a structural advantage that allows for a higher FoM even at lower Ag NW densities. In other words, the welding process not only reduces the contact resistance but also shifts the dominant performance factor from sheet resistance to transmittance, thereby enabling a high FoM while minimizing the quantity of Ag NWs used. This strongly suggests a strategic approach for next-generation transparent electrode design that simultaneously achieves material efficiency and performance optimization.

To elucidate how the welding process reorganizes the dominant factors of the FoM for the TCE, the conductive network of the hybrid electrode can be analyzed based on eqn (1) using a log–log plot of $(1/\sqrt{T}-1)$ *versus* R_s, as shown in Fig. 6. The slopes of the fitted lines in Fig. 6 represent the results of quantifying the electrical and optical properties of the hybrid electrode based on percolation theory, as encapsulated in eqn (2). Specifically, the slope of the log–log plot in Fig. 6 is defined as $-1/(n+1)$, where n is the percolation exponent, and the magnitude of this value can be used to distinguish whether the electrode behavior falls within the percolative or bulk regime.[32] Generally, a slope of −1 indicates that bulk behavior is dominant, while a decrease in the absolute value of the slope ($|\text{slope}| < 1$) is interpreted as a strengthening of the percolative behavior.[33] When the conductive pathways are discontinuous, Π is dominated by changes in the sheet resistance, thereby characterizing the percolative regime; conversely, when a continuous network is sufficiently formed, the system transitions to the bulk regime, where Π is primarily influenced by changes in transmittance.[33] Because the critical point for the percolative-to-bulk transition may vary somewhat depending on the electrode structure and properties, a slope more negative than −1 could be interpreted as enhanced bulk behavior.[34–36] Thus, in Fig. 6a, the slope of $(1/\sqrt{T}-1)$ *versus* R_s for the non-welded hybrid electrodes is generally distributed in the range of −0.7 to −1.0, which indicates a dominant percolative behavior. After welding, however, the slope shifts toward the −1.3 to −2.3 range (Fig. 6b), thereby confirming that the bulk behavior is enhanced in all hybrid electrodes. This change demonstrates that the welding process effectively reduces the contact resistance between Ag NWs, thereby stabilizing the conductive pathways. Additionally, in Fig. 6a and b, the slopes for samples with high Ag NW densities (Ag1000–3000, represented by the filled symbols) are clearly distinguishable from those of samples with low densities (Ag4000–6000, open symbols), which is consistent with the behavioral transition near the percolation threshold (*i.e.*, in the Ag3000–4000 range) observed in Fig. S3.

In brief, the results of this study clearly demonstrate that the welding process shifts the behavior of the hybrid electrode from the percolative regime to the bulk regime. For this reason, after welding, the sheet resistance of the hybrid electrode is almost completely unaffected by the density of Ag NWs, such that the dominant factor affecting the FoM of the TCE is shifted from sheet resistance to transmittance. Therefore, this study proves that the welding process has effects beyond simply reducing the contact resistance and that it is a critical step that restructures the performance-determining factors of the hybrid electrode, thereby enabling the simultaneous achievement of material efficiency and enhanced optical performance.

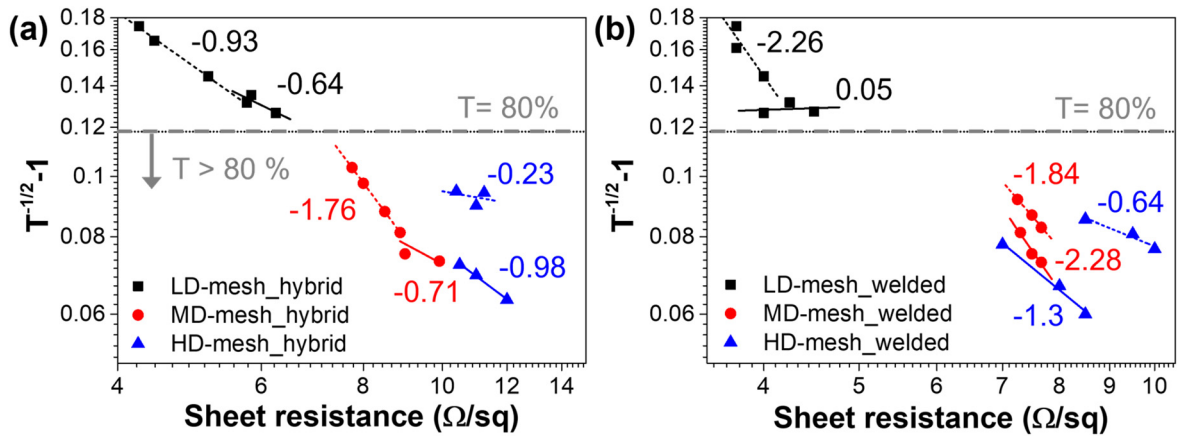

Fig. 6 The log–log plots of $(1/\sqrt{T}-1)$ *vs.* R_s for the various hybrid electrodes (a) before and (b) after welding, where the samples with high Ag NW densities (Ag1000–3000) are represented by the filled symbols and those with low Ag NW densities (Ag4000–6000) are represented by the open symbols. The numbers indicate the slope of each curve, with shallower slopes corresponding to percolative behavior, while steeper slopes represent bulk-like transport.

Open Access Article. Published on 13 May 2026. Downloaded on 6/28/2026 9:54:55 AM.
This article is licensed under a Creative Commons Attribution-NonCommercial 3.0 Unported Licence.

Conclusions

Herein, the operating mechanism of the conductive network and the performance-dominant factors of the figure of merit (FoM) were systematically investigated for hybrid electrodes combining a silver (Ag) micro-mesh and Ag nanowires (NWs). The analysis revealed that as the density of Ag NWs decreases, the hybrid electrode exhibits typical percolation behavior characterized by a reduction in conductive pathways and an increase in sheet resistance. This indicates that the primary factor limiting the electrode performance is the contact resistance between NW–NW and NW–mesh junctions. To overcome these limitations, a low-temperature (200 °C) welding process was applied for 10 min, after which the sheet resistance of the hybrid electrode was found to be independent of the Ag NW density. Moreover, this welding process not only reduced the contact resistance but also transformed the conduction behavior from a percolative regime to a bulk regime. This transition in conduction behavior provided a decisive turning point, which reorganized the FoM of the TCE from being sheet resistance-centered to transmittance-centered. Notably, after welding, the hybrid sample with a high-density (HD) mesh and 6000 rpm spin-coated Ag NWs achieved a sheet resistance of 7.0 Ω sq^{-1} and a transmittance of 86.1%, thus resulting in a high FoM value of 373. These electrical and optical performance properties are comparable to those of conventional indium tin oxide (ITO) electrodes. The excellent performance of this hybrid electrode was achieved by the simultaneous stabilization of conductive pathways *via* the welding process and maximization of the optical transmittance due to the low density of Ag NWs. Furthermore, the behavioral differences according to the changes in Ag NW density were systematically elucidated in order to demonstrate the importance of density control and contact engineering in the design of hybrid electrodes. This study successfully optimized the structure and characteristics of hybrid electrodes beyond the use of simple material combinations by introducing the concept of reorganizing the performance-dominant factors *via* a mode transition in the network conduction behavior. Based on this principle, a TCE design strategy and feasible processing method were proposed that can be effectively used in various next-generation applications such as flexible displays, transparent solar cells, and wearable electronic devices.

Author contributions

Seung Taek Jo: conceptualization, formal analysis, visualization, and writing – original draft; Chan Woong Kim: investigation; Jin Wook Shin: conceptualization, investigation, and visualization; Gyeongtae Kim: investigation; Dongrim Lee: investigation; Dae-Hwang Yoo: supervision; Hyesun Yoo: supervision and writing – review & editing; Jong Wook Roh: supervision, project administration, writing – review & editing and funding acquisition.

Conflicts of interest

There are no conflicts to declare.

Data availability

The data supporting this article have been included as part of the supplementary information (SI). Supplementary information: Fig. S1–S4 and Table S1, SEM and AFM images and further experimental results and details. See DOI: https://doi.org/10.1039/d6nr00517a.

Acknowledgements

This research was supported by the National Research Foundation of Korea (NRF), funded by the Ministry of Science and ICT (MSIT) (No. RS-2021-NR060108 and RS-2023-00249229).

References

1 H. Yu, Y. Tian, M. Dirican, D. Fang, C. Yan, J. Xie, D. Jia, Y. Liu, C. Li and M. Cui, Flexible, transparent and tough silver nanowire/nanocellulose electrodes for flexible touch screen panels, *Carbohydr. Polym.*, 2021, **273**, 118539.
2 S. Yang, Y.-J. Cao, K. Han, J.-T. Guo, P.-L. Zheng, L.-Y. Wang, T. Cheng, Y.-Z. Zhang and W.-Y. Lai, Stretchable transparent electrodes based on metal grid hybrids for skin-like multimodal sensing and flexible touch panel, *Nano Energy*, 2025, **139**, 110942.
3 H. Yoo, H. Van Quy, I. Lee, S. T. Jo, T. E. Hong, J. Kim, D. H. Yoo, J. Shin, W. Commerell and D. H. Kim, Understanding of the Relationship between the Properties of Cu (In, Ga) Se2 Solar Cells and the Structure of Ag Network Electrodes, *Energy Environ. Mater.*, 2024, **7**, e12765.
4 S. T. Jo, J. W. Shin, M.-S. Kim, S.-S. Park, W. Commerell, H. Yoo, J. Hwang and J. W. Roh, Optimized electrical and optical properties of Ag micro-meshes by self-generated cracks for transparent electrodes, *J. Mater. Chem. C*, 2025, **13**, 9309–9316.
5 B. Sun, R. Xu, X. Han, J. Xu, W. Hong, Y. Xu, Z. Fu, H. Zhu, X. Sun and J. Wang, Ultra-high temperature tolerant flexible transparent electrode with embedded silver nanowires bundle micromesh for electrical heater, *npj Flexible Electron.*, 2022, **6**, 48.
6 S.-s. Li, Y.-l. Wang, B.-j. Li, L.-j. Huang and N.-f. Ren, Copper/silver composite mesh transparent electrodes with low reflection for high-performance and low-voltage transparent heaters, *J. Alloys Compd.*, 2021, **865**, 158877.
7 K. Zhang, L. Meng, M. Zhang, Y. Li, L. Jiang and H. Liu, An ultra–high transparent electrode via a unique micro–patterned AgNWs crossing–network with 3.9% coverage: toward highly–transparent flexible QLEDs, *Adv. Funct. Mater.*, 2024, **34**, 2308468.

Open Access Article. Published on 13 May 2026. Downloaded on 6/28/2026 9:54:55 AM. This article is licensed under a Creative Commons Attribution-NonCommercial 3.0 Unported Licence.

8 J. Wang, J. Fan, T. Wan, L. Hu, Z. Li and D. Chu, Recent Progress in Silver Nanowire–Based Transparent Conductive Electrodes, *Adv. Energy Sustainability Res.*, 2025, 2500033.
9 H. Li, D. Zi, X. Zhu, H. Zhang, Y. Tai, R. Wang, L. Sun, Y. Zhang, W. Ge and Y. Huang, Electric field driven printing of repeatable random metal meshes for flexible transparent electrodes, *Opt. Laser Technol.*, 2023, **157**, 108730.
10 S. Yuan, Z. Fan, G. Wang, Z. Chai, T. Wang, D. Zhao, A. A. Busnaina and X. Lu, Fabrication of Flexible and Transparent Metal Mesh Electrodes Using Surface Energy–Directed Assembly Process for Touch Screen Panels and Heaters, *Adv. Sci.*, 2023, **10**, 2304990.
11 D. A. Ilatovskii, E. P. Gilshtein, O. E. Glukhova and A. G. Nasibulin, Transparent conducting films based on carbon nanotubes: rational design toward the theoretical limit, *Adv. Sci.*, 2022, **9**, 2201673.
12 W. Jang, B. G. Kim, S. Seo, A. Shawky, M. S. Kim, K. Kim, B. Mikladal, E. I. Kauppinen, S. Maruyama and I. Jeon, Strong dark current suppression in flexible organic photodetectors by carbon nanotube transparent electrodes, *Nano Today*, 2021, **37**, 101081.
13 Y. Zhou and R. Azumi, Carbon nanotube based transparent conductive films: progress, challenges, and perspectives, *Sci. Technol. Adv. Mater.*, 2016, **17**, 493–516.
14 H. B. Lee, W.-Y. Jin, M. M. Ovhal, N. Kumar and J.-W. Kang, Flexible transparent conducting electrodes based on metal meshes for organic optoelectronic device applications: a review, *J. Mater. Chem. C*, 2019, **7**, 1087–1110.
15 F. Selzer, C. Floresca, D. Kneppe, L. Bormann, C. Sachse, N. Weiß, A. Eychmüller, A. Amassian, L. Müller-Meskamp and K. Leo, Electrical limit of silver nanowire electrodes: Direct measurement of the nanowire junction resistance, *Appl. Phys. Lett.*, 2016, **108**, 163302.
16 T. Ye, L. Jun, L. Kun, W. Hu, C. Ping, D. Ya-Hui, C. Zheng, L. Yun-Fei, W. Hao-Ran and D. Yu, Inkjet-printed Ag grid combined with Ag nanowires to form a transparent hybrid electrode for organic electronics, *Org. Electron.*, 2017, **41**, 179–185.
17 J. Jang, H.-G. Im, J. Jin, J. Lee, J.-Y. Lee and B.-S. Bae, A flexible and robust transparent conducting electrode platform using an electroplated silver grid/surface-embedded silver nanowire hybrid structure, *ACS Appl. Mater. Interfaces*, 2016, **8**, 27035–27043.
18 H. Yang, Y. Bi, S. Wang, C. Wang, H. Wang, G. Ye and J. Feng, Ag-Grid and Ag-Nanowires Hybrid Transparent Electrodes to Improve Performance of Flexible Organic Light-Emitting Devices, in *Photonics*, MDPI, 2025, pp. 272.
19 T. Ye, L. Jun, L. Kun, W. Hu, C. Ping, D. Ya-Hui, C. Zheng, L. Yun-Fei, W. Hao-Ran and D. Yu, Inkjet-printed Ag grid combined with Ag nanowires to form a transparent hybrid electrode for organic electronics, *Org. Electron.*, 2017, **41**, 179–185.
20 M. W. Knight, J. van de Groep, P. C. Bronsveld, W. C. Sinke and A. Polman, Soft imprinted Ag nanowire hybrid electrodes on silicon heterojunction solar cells, *Nano Energy*, 2016, **30**, 398–406.
21 X. Xu, Z. Liu, P. He and J. Yang, Screen printed silver nanowire and graphene oxide hybrid transparent electrodes for long-term electrocardiography monitoring, *J. Phys. D: Appl. Phys.*, 2019, **52**, 455401.
22 S. J. Kim, H. G. Yoon and S. W. Kim, Extremely robust and reliable transparent silver nanowire–mesh electrode with multifunctional optoelectronic performance through selective laser nanowelding for flexible smart devices, *Adv. Eng. Mater.*, 2021, **23**, 2001310.
23 L. Wang, Y. Wang, F. Ning, H. Zhou, H. Wang and G.-S. Liu, *Cross-Aligned, Plasma-Welded Silver Nanowire Networks for High-Performance Flexible Transparent Electrodes, Surfaces and Interfaces*, 2025, 107036.
24 L. Jongsoo, W. J. Yeon, K. J. Tae, L. B. Yang and H. Chang-Soo, *Synergistically Enhanced Stability of Highly Flexible Silver Nanowire/Carbon Nanotube Hybrid Transparent Electrodes by Plasmonic Welding*, 2014.
25 R. E. Triambulo, H.-G. Cheong and J.-W. Park, All-solution-processed foldable transparent electrodes of Ag nanowire mesh and metal matrix films for flexible electronics, *Org. Electron.*, 2014, **15**, 2685–2695.
26 Y. Liu, J. Zhang, H. Gao, Y. Wang, Q. Liu, S. Huang, C. F. Guo and Z. Ren, Capillary-force-induced cold welding in silver-nanowire-based flexible transparent electrodes, *Nano Lett.*, 2017, **17**, 1090–1096.
27 T. L. Chen, D. S. Ghosh, V. Mkhitaryan and V. Pruneri, Hybrid transparent conductive film on flexible glass formed by hot-pressing graphene on a silver nanowire mesh, *ACS Appl. Mater. Interfaces*, 2013, **5**, 11756–11761.
28 F. Xu, W. Xu, B. Mao, W. Shen, Y. Yu, R. Tan and W. Song, Preparation and cold welding of silver nanowire based transparent electrodes with optical transmittances >90% and sheet resistances <10 ohm/sq, *J. Colloid Interface Sci.*, 2018, **512**, 208–218.
29 D. Langley, M. Lagrange, G. Giusti, C. Jiménez, Y. Bréchet, N. D. Nguyen and D. Bellet, Metallic nanowire networks: effects of thermal annealing on electrical resistance, *Nanoscale*, 2014, **6**, 13535–13543.
30 S. De, T. M. Higgins, P. E. Lyons, E. M. Doherty, P. N. Nirmalraj, W. J. Blau, J. J. Boland and J. N. Coleman, Silver nanowire networks as flexible, transparent, conducting films: extremely high DC to optical conductivity ratios, *ACS Nano*, 2009, **3**, 1767–1774.
31 Y. Yang, S. Duan and H. Zhao, Advances in constructing silver nanowire-based conductive pathways for flexible and stretchable electronics, *Nanoscale*, 2022, **14**, 11484–11511.
32 S. De, P. J. King, P. E. Lyons, U. Khan and J. N. Coleman, Size effects and the problem with percolation in nanostructured transparent conductors, *ACS Nano*, 2010, **4**, 7064–7072.
33 S. Sorel, D. Bellet and J. N. Coleman, Relationship between material properties and transparent heater performance for both bulk-like and percolative nanostructured networks, *ACS Nano*, 2014, **8**, 4805–4814.
34 R. M. Mutiso, M. C. Sherrott, A. R. Rathmell, B. J. Wiley and K. I. Winey, Integrating simulations and experiments

Open Access Article. Published on 13 May 2026. Downloaded on 6/28/2026 9:54:55 AM.
This article is licensed under a Creative Commons Attribution-NonCommercial 3.0 Unported Licence.

to predict sheet resistance and optical transmittance in nanowire films for transparent conductors, *ACS Nano*, 2013, **7**, 7654–7663.

35 S. Kirkpatrick, Percolation and conduction, *Rev. Mod. Phys.*, 1973, **45**, 574–588.

36 S.-I. Lee, Y. Song, T. W. Noh, X.-D. Chen and J. R. Gaines, Experimental observation of nonuniversal behavior of the conductivity exponent for three-dimensional continuum percolation systems, *Phys. Rev. B:Condens. Matter Mater. Phys.*, 1986, **34**, 6719–6724.